CrossMark

Fundamental Limits of TOA/DOA and Inertial Measurement Unit-Based Wireless Capsule Endoscopy Hybrid Localization

Seongah Jeong[1] · Joonhyuk Kang[2] · Kaveh Pahlavan[3] · Vahid Tarokh[1]

Abstract In this paper, performance analysis of hybrid localization based on radio-frequency (RF) and inertial measurement unit (IMU) measurements for a single wireless capsule endoscopy (WCE) traveling the gastrointestinal tract is studied. Specifically, the multiple body-mounted sensors are considered which are located on the front and back of a patient's medical jacket and form the uniform rectangular arrays (URAs). With the aim of locating the WCE, two types of RF measurements, namely time-of-arrival (TOA) and direction-of-arrival (DOA), are estimated from the received signals at the URAs transmitted by the WCE, which are integrated with the IMU acceleration measurements via the standard extended Kalman filter. Here, a posterior Cramér–Rao Bound (PCRB) of the proposed TOA/DOA and IMU-based hybrid localization is derived as fundamental limits on squared position error, where the accuracies of TOA and DOA measurements are entailed by means of CRB to account for their dependency on the environmental parameters, while the accuracies of the IMU measurements are addressed with the acceleration measurement error standard deviation. Numerical results are provided, sustained by simulations which verify the millimeter accuracy of the TOA/DOA and IMU-based hybrid localization within the regulation of medical implant communication services and the exactness of the PCRB.

1 Introduction

Wireless capsule endoscopy (WCE) has emerged as a leading technology for diagnostic of gastrointestinal (GI) and mucosal diseases without risk of side effects of the traditional endoscopy such as breath difficulty, perforation or tearing of the intestinal wall, post-procedural infection and vomiting during the examination [1, 2]. Generally, the WCE refers to a swallowable pill-size medical device to be equipped with a tiny camera and illuminating systems to capture the images of the interior of GI tract; radio frequency (RF) transmission module to transmit the images and RF signals to receivers located on or outside the body; and a battery [3].

In order to facilitate the accurate diagnosis, the WCE localization techniques are essential associated with the captured image. They can be largely grouped into magnetic-based [4, 5], image-based [6, 7] and RF-based methods [8–10], each of which has challenging issues for implementation. In particular, the magnetic-based methods are highly sensitive to the distance between the WCE and

✉ Seongah Jeong
  sej293@g.harvard.edu

  Joonhyuk Kang
  jhkang@ee.kaist.ac.kr

  Kaveh Pahlavan
  kaveh@wpi.edu

  Vahid Tarokh
  vahid@seas.harvard.edu

[1] School of Engineering and Applied Sciences, Harvard University, Cambridge, MA 02138, USA

[2] Department of Electrical Engineering, KAIST, Daejeon 34141, Republic of Korea

[3] Department of Electrical and Computer Engineering, Worcester Polytechnic Institute, Worcester, MA 01609, USA

Springer

sensors when the permanent magnets are used [4], or require an external energy resources to excite the magnetic field when the electromagnetic waves are used [5]. In the image-based WCE localization [6, 7], the low image quality and frame rate caused by the constrained transmit power of the WCE degrade the localization performance. With the benefits of low hardware cost and applicability as well as with the rapid technical developments by the increasing interests on location-awareness in cellular networks [11–14], the RF-based methods have gained attention for the WCE localization via time-of-arrival (TOA) [8, 9], time-difference-of-arrival (TDOA) [9], direction-of-arrival (DOA) [10] or received signal strength (RSS) [8] measurements. Nevertheless, the difficulties exist for in-body tracking using RF signals due to the uniqueness of body area networks, e.g., the inconsistency of RSS attenuation, propagation and refraction inside the body and the restrictions on the use of high bandwidth and on transmit power. To address these challenging issues, the hybrid localization techniques are introduced by using the multiple types of RF measurements and, by extension, combining RF measurements with other types of position-related measurements [8–10].

In this paper, we develop the hybrid localization based on the RF and inertial measurement unit (IMU) measurements for a single WCE traveling the GI tract and derive its fundamental limits of localization accuracy in terms of a performance measure called the squared position error (SPE). To this end, the multiple body-mounted sensors are considered which are located on the front and back of a patient's jacket during the examination and form the uniform rectangular arrays (URAs) as shown in Fig. 1. The WCE is assumed to be equipped with the IMU to enable its acceleration measurements in the body reference frame. With the goal of locating the WCE, two types of RF measurements, namely TOA and DOA, are estimated at the URAs from the received signals transmitted by the WCE,

which are then integrated with the IMU acceleration measurements via the standard extended Kalman filter (EKF). Differently from the prior works on the hybrid RF and IMU-based localization [9, 10], we analytically derive the fundamental limits on squared position error (SPE) of the proposed scheme by adopting a Posterior Cramér–Rao bound (PCRB). In the derivation, the accuracies of TOA and DOA measurements are taken into account by means of CRB to reflect their dependency on environmental parameters, while the accuracies of IMU measurements are entailed with the acceleration measurement error standard deviation. Numerical results are provided via simulations, which corroborate the exactness of the PCRB. Moreover, it is validated that the millimeter accuracy of the proposed TOA/DOA and IMU-based hybrid localization can be obtained within the medical implant communication services (MICS) regulation, which outperforms all the reference WCE localization schemes such as only RF (TOA/DOA)-based, only IMU-based, and hybrid RF and IMU-based schemes using only one type of RF measurements, i.e., either TOA or DOA.

The rest of this paper is organized as follows. Section 2 presents the system model including the measurement and dynamic model of the proposed scheme. In Sect. 3, we design the TOA/DOA and IMU-based WCE hybrid localization via the EKF, and then derive its PCRB in Sect. 4. Numerical results are given in Sect. 5, and conclusions are finally drawn in Sect. 6.

2 System and Signal Model

We consider a TOA/DOA and IMU-based WCE hybrid localization system as illustrated in Fig. 1. We consider NM sensors which are mounted on the front and back side of the patient's jacket to form the URA configuration with a three dimensional range of $L_W \times L_L \times L_H$ cm. For the

Fig. 1 Illustration of the considered set-up
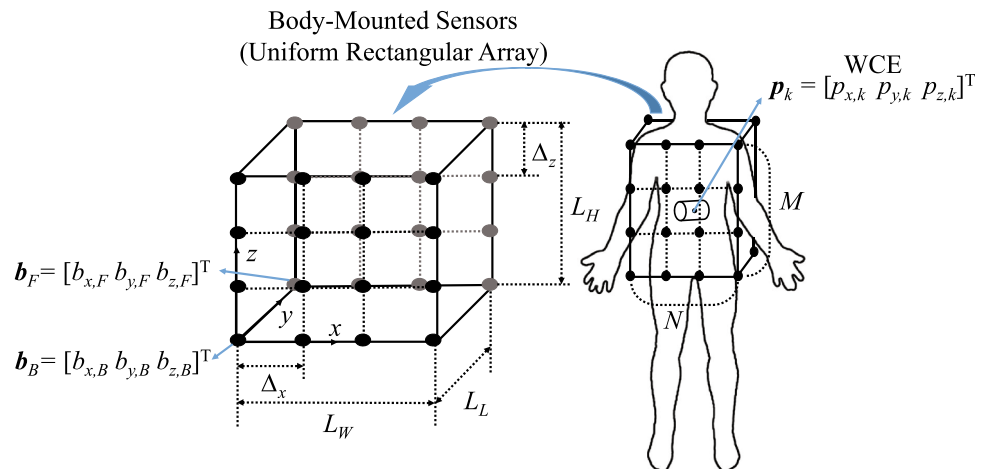
URAs, the inter-element distances along side the x and z axes are denoted as Δ_x and Δ_z, and their reference positions are given as $\boldsymbol{b}_F = [b_{x,F} \ b_{y,F} \ b_{z,F}]^T$ for the front and $\boldsymbol{b}_B = [b_{x,B} \ b_{y,B} \ b_{z,B}]^T$ for the back, respectively, which are assumed to be perfectly known. The URAs communicate with the transmitter within the WCE moving along a trajectory $\boldsymbol{p}(t) = [p_x(t) \ p_y(t) \ p_z(t)]^T$ of the GI tract from the mouth to rectum for $t \geq 0$. The observation time is assumed to be partitioned into slots of duration δ seconds, by which the WCE's trajectory $\boldsymbol{p}(t)$ can be sampled as $\boldsymbol{p}_k = [p_{x,k} \ p_{y,k} \ p_{z,k}]^T \triangleq \boldsymbol{p}(k\delta)$. We assume that the direct signal can be resolvable, and the WCE and sensors are synchronized, which allows us to obtain the TOA and DOA measurements from the received signals at URAs. Note that the asynchronism between the WCE and sensors may be accounted by following the same approach in [11], where the TDOA measurements can be applied in lieu of TOA measurements, and we leave it for future work. We also assume no patient's body motion during the examination since the estimation error due to the patient's movement can be compensated by motion tracking via the additional transmitters installed on the body, specially shoulder or waist level [9]. Moreover, the WCE is assumed to be equipped with the IMU to enable its acceleration measurement in the body reference frame.

Under the above assumptions, the discrete-time received signal of the URA $i \in \{F, B\}$ at the kth time slot can be written as

$$\boldsymbol{r}_{k,i} = h_{k,i} \alpha(\theta_{k,i}, \phi_{k,i}) s(k\delta - \tau_{k,i}) + \boldsymbol{n}_{k,i}, \tag{1}$$

where $s(t)$ is a known signal to all the nodes with an unit energy; $\boldsymbol{n}_{k,i} \triangleq \boldsymbol{n}_i(k\delta)$ with $\boldsymbol{n}_i(t)$ being the noise modeled zero-mean additive white Gaussian processes at the URA i with two-side power spectral density N_0; and $h_{k,i} = h_{k,i}^L h_{k,i}^S$ is the amplitude of direct path between the WCE and URA i at the time slot k with the large-scale fading coefficients $h_{k,i}^L$ and the small-scale fading coefficients $h_{k,i}^S$. Here, the power of large-scale fading coefficients follows the standard channel model of IEEE 802.15.6 at MICS band [15] and is given as

$$\left| h_{k,i}^L \right|^2 = P_t - PL(d_0) - 10\mu \log_{10}(d_{k,i}/d_0) + N, \tag{2}$$

where P_t is the WCE's constant transmit power; $PL(d_0)$ is the pathloss at a reference distance d_0 cm; $d_{k,i}$ is the Euclidean distance between the the kth WCE state and URA i; N is a zero-mean Gaussian random variable with the variance σ_s^2 to represent the shadowing effect; and μ is the pathloss exponent, whose specifications are summarized in Table 1 when $d_0 = 5$ cm is considered [16]. Moreover, in (1), $\tau_{k,i}$ and $\alpha(\theta_{k,i}, \phi_{k,i})$ represent the

Table 1 Parameters for the implant to body surface pathloss model

Implant to body surface	$PL(d_0)$ (dB)	μ	σ_s
Deep tissue ($d_{k,i} > 10$ cm)	47.14	4.26	7.85
Near tissue ($d_{k,i} \leq 10$ cm)	49.81	4.22	6.81

propagation delay and array response of direct path between the kth WCE state and URA i, respectively, which are defined as

$$\tau_{k,i} = \frac{d_{k,i}}{c_{\text{avg}}} = \frac{1}{c_{\text{avg}}} \|\boldsymbol{p}_k - \boldsymbol{b}_i\|, \tag{3a}$$

$$\alpha(\theta_{k,i}, \phi_{k,i}) = \alpha_x(\theta_{k,i}, \phi_{k,i}) \otimes \alpha_z(\phi_{k,i}), \tag{3b}$$

where $c_{\text{avg}} = c/\sqrt{\epsilon_{\text{avg}}}$ is the propagation speed with the speed of light c and the average relative permittivity ϵ_{avg} [8]; $\otimes$ is the Kronecker product; and the azimuth steering vector $\alpha_x(\theta_{k,i}, \phi_{k,i})$ and elevation steering vector $\alpha_z(\phi_{k,i})$ are given as

$$\alpha_x(\theta_{k,i}, \phi_{k,i}) = \left[1 \ e^{j\frac{2\pi}{\lambda}\Delta_x \cos\theta_{k,i} \cos\phi_{k,i}} \ \cdots \ e^{j\frac{2\pi}{\lambda}\Delta_x(N-1)\cos\theta_{k,i}\cos\phi_{k,i}}\right]^T, \tag{4a}$$

$$\alpha_z(\phi_{k,i}) = \left[1 \ e^{j\frac{2\pi}{\lambda}\Delta_z \sin\phi_{k,i}} \ \cdots \ e^{j\frac{2\pi}{\lambda}\Delta_z(M-1)\sin\phi_{k,i}}\right]^T, \tag{4b}$$

with λ being the wavelength, and $\theta_{k,i}$ and $\phi_{k,i}$ being the the azimuth angle and elevation angle, respectively, which are defined based on trigonometric equations [17] with respect to the positive x-axis and xy-plain as

$$\theta_{k,i} = \tan^{-1}\left(\frac{p_{y,k} - b_{y,i}}{p_{x,k} - b_{x,i}}\right), \tag{5a}$$

$$\phi_{k,i} = \tan^{-1}\left(\frac{p_{z,k} - b_{z,i}}{\sqrt{(p_{x,k} - b_{x,i})^2 + (p_{y,k} - b_{y,i})^2}}\right). \tag{5b}$$

2.1 Measurement Model

For the TOA measurements $\tau_{k,i}$ in (3a) and DOA measurements $\{\theta_{k,i}, \phi_{k,i}\}$ in (5) obtained at the URA i at the kth time slot, we can write the measurement model as

$$\boldsymbol{y}_{k,i} = [\tau_{k,i} \ \theta_{k,i} \ \phi_{k,i}]^T + \boldsymbol{z}_{k,i}, \tag{6}$$

where $\boldsymbol{z}_{k,i}$ is the zero-mean Gaussian white measurement noise with the covariance matrix $\boldsymbol{Z}_{k,i} = E\{\boldsymbol{z}_{k,i}\boldsymbol{z}_{k,i}^T\}$. In order to compute the matrix $\boldsymbol{Z}_{k,i}$, we use the classical CRB [18] based on the received signal $\boldsymbol{r}_{k,i}$ in (1), where the dependency of the accuracies of RF measurements on environmental parameters is entailed. The error variance $\sigma_{\tau_{k,i}}^2$ for the TOA estimation $\tau_{k,i}$ can be calculated as

$$\sigma_{\tau_{k,i}}^2 = \frac{1}{8\pi^2\beta^2 MN\mathrm{SNR}_{k,i}}, \tag{7}$$

where $\beta = (\int_{-\infty}^{\infty} |fS(f)|^2 df)^{1/2}$ is the effective bandwidth; and $\mathrm{SNR}_{k,i} = |h_{k,i}|^2/N_0$ is the signal-to-noise ratio for the direct path between the kth WCE's location and URA i. The error variances $\sigma_{\theta_{k,i}}^2$ and $\sigma_{\phi_{k,i}}^2$ for the DOA estimation $\theta_{k,i}$ and $\phi_{k,i}$, respectively, can be given as

$$\sigma_{\theta_{k,i}}^2 = \frac{3\lambda^2}{4\pi^2 \Delta_x^2 \sin^2\theta_{k,i}\cos^2\phi_{k,i} MN(N-1)(2N-1)\mathrm{SNR}_{k,i}}, \tag{8a}$$

$$\sigma_{\phi_{k,i}}^2 = \frac{\lambda^2}{4\pi^2 MN\mathrm{SNR}_{k,i}}\left(\frac{\Delta_x^2\cos^2\theta_{k,i}\sin^2\phi_{k,i}(N-1)(2N-1)}{3}\right.$$
$$-\Delta_x\Delta_z\cos\theta_{k,i}\sin\phi_{k,i}\cos\phi_{k,i}(M-1)(N-1)$$
$$\left.+\frac{\Delta_z^2\cos^2\phi_{k,i}(M-1)(2M-1)}{3}\right)^{-1}. \tag{8b}$$

The error variances $\sigma_{\tau_{k,i}}^2, \sigma_{\theta_{k,i}}^2$ and $\sigma_{\phi_{k,i}}^2$ can be easily derived by following [11, 12, 14, 18] whose details are not discussed here. By following [8, 9], the TOA and DOA measurements are assumed to be independent, by which the measurement covariance matrix $\mathbf{Z}_{k,i}$ is then represented as

$$\mathbf{Z}_{k,i} = \mathrm{diag}\{\sigma_{\tau_{k,i}}^2, \sigma_{\theta_{k,i}}^2, \sigma_{\phi_{k,i}}^2\}. \tag{9}$$

2.2 Dynamic Model

Next, we consider the WCE's dynamic model. The digestion system is known to have an irregular and variable shape, which makes it difficult to model the WCE's mobility.

To address this problem, by considering that the sampling rate for the WCE's position is no more than one second, i.e., $\delta \leq 1$, we assume the linear motion of the WCE [9]. As a result, we have the kth state vector $\mathbf{x}_k = [\mathbf{p}_k^T \ \mathbf{v}_k^T]^T$ with the velocity vector $\mathbf{v}_k = [v_{x,k} \ v_{y,k} \ v_{z,k}]^T$ to follow the state equations:

$$\mathbf{x}_{k+1} = \mathbf{A}\mathbf{x}_k + \mathbf{B}\mathbf{u}_k + \mathbf{G}\mathbf{w}_k, \tag{10}$$

where the transition matrix $\mathbf{A}$ and the control input matrix $\mathbf{B}$ are calculated as

$$\mathbf{A} = \begin{bmatrix} \mathbf{I}_{3\times3} & \delta\mathbf{I}_{3\times3} \\ \mathbf{0}_{3\times3} & \mathbf{I}_{3\times3} \end{bmatrix} \quad \text{and} \quad \mathbf{B} = \begin{bmatrix} \frac{1}{2}\delta^2\mathbf{I}_{3\times3} \\ \delta\mathbf{I}_{3\times3} \end{bmatrix}, \tag{11}$$

respectively; $\mathbf{G}$ is a projection matrix to project the process noise into the state vector; $\mathbf{w}_k$ is zero-mean Gaussian white

process noise with the covariance matrix $\mathbf{W}_k = E\{\mathbf{w}_k\mathbf{w}_k^T\}$; and $\mathbf{u}_k = [u_{x,k} \ u_{y,k} \ u_{z,k}]^T$ denotes the IMU measurement vector, i.e., the measured acceleration of the WCE, which is expressed as

$$\mathbf{u}_k = \mathbf{a}_k - \mu_b + \mu_u, \tag{12}$$

with $\mathbf{a}_k = [a_{x,k} \ a_{y,k} \ a_{z,k}]^T$ being the true acceleration of WCE, μ_b being the IMU drift bias, and μ_u being the IMU measurement noise consisting of zero-mean Gaussian random variables with the variance $\sigma_{\mu_u}^2$. We assume that the WCE's biases can be calculated via calibration process before the inspection, which allows us to consider only the effect of the IMU measurement noise μ_u.

3 TOA/DOA and IMU-Based WCE Hybrid Localization via EKF

In this section, we design the TOA/DOA and IMU-based WCE hybrid localization via the standard EKF. The EKF is conventionally adopted for the nonlinear observation and dynamic model to forecast the next estimate using the first-order error approximation via Taylor Series. By applying the EKF to incorporate the TOA, DOA and IMU measurements, we estimate the WCE's location whose details are discussed in the following.

Using the measurement model (6) and dynamic model (10), the system state transition function is represented as

$$\mathbf{x}_{k+1} = \mathbf{A}\mathbf{x}_k + \mathbf{B}\mathbf{u}_k + \mathbf{G}\mathbf{w}_k, \tag{13a}$$

$$\mathbf{y}_{k+1} = \mathbf{h}(\mathbf{x}_{k+1}) + \mathbf{z}_{k+1}, \tag{13b}$$

where $\mathbf{w}_k$ and $\mathbf{z}_{k'}$ are assumed to be uncorrelated so that $E\{\mathbf{w}_k\mathbf{z}_{k'}^T\} = 0$ for all k and k'. In (13b), $\mathbf{h}(\cdot)$ is the observation nonlinear vector function that yields the TOA and DOA measurements of all the URAs from the WCE's state predicted by IMU measurements. We define $\mathbf{y}_k = [\mathbf{y}_{k,F}^T \ \mathbf{y}_{k,B}^T]^T$ and $\mathbf{z}_k = [\mathbf{z}_{k,F}^T \ \mathbf{z}_{k,B}^T]^T$ with the covariance matrix $\mathbf{Z}_k = \mathrm{diag}\{\mathbf{Z}_{k,F}, \mathbf{Z}_{k,B}\}$ by collecting all the corresponding vectors of URAs related to the kth WCE's state. The WCE's initial state $\mathbf{x}_0 = \mathbf{x}_0^{\mathrm{u}} = \mu_x$ is given at the patient's mouth with the known mean $E\{\mathbf{x}_0\} = \mu_x$ and covariance matrix $\mathbf{P}_0 = E\{(\mathbf{x}_0 - \mu_x)(\mathbf{x}_0 - \mu_x)^T\}$. The summary of the TOA/DOA and IMU-based hybrid localization is shown in Algorithm 1.

In particular, at each kth iteration, the WCE's next state $\mathbf{x}_{k+1}^{\mathrm{p}}$ and covariance $\mathbf{P}_{k+1}^{\mathrm{p}}$ predicted by the IMU measurement $\mathbf{u}_k$ are given as

$$\mathbf{x}_{k+1}^{\mathrm{p}} = \mathbf{A}\mathbf{x}_k^{\mathrm{u}} + \mathbf{B}\mathbf{u}_k, \tag{14a}$$

$$\mathbf{P}_{k+1}^{\mathrm{p}} = \mathbf{A}\mathbf{P}_k\mathbf{A}^T + \mathbf{Q}, \tag{14b}$$

respectively, where the matrix $\boldsymbol{Q} = \boldsymbol{G}\boldsymbol{W}_k\boldsymbol{G}^T$ is the desired process noise covariance matrix in (13a) and is computed based on the continuous-time model of (14a) as [9, 10, 19]

$$\boldsymbol{Q} = \sigma_{\mu_u}^2 \begin{bmatrix} \dfrac{\delta^3}{3}\boldsymbol{I}_{3\times3} & \dfrac{\delta^2}{2}\boldsymbol{I}_{3\times3} \\ \dfrac{\delta^2}{2}\boldsymbol{I}_{3\times3} & \delta\boldsymbol{I}_{3\times3} \end{bmatrix}, \tag{15}$$

which depends on the variance $\sigma_{\mu_u}^2$ of IMU measurement noise μ_u.

Then, the Kalman gain $\boldsymbol{K}_{k+1}$ is calculated as

$$\boldsymbol{K}_{k+1} = \boldsymbol{P}_{k+1}^{\mathrm{p}}\boldsymbol{H}^T(\boldsymbol{x}_{k+1}^{\mathrm{p}})\big(\boldsymbol{H}(\boldsymbol{x}_{k+1}^{\mathrm{p}})\boldsymbol{P}_{k+1}^{\mathrm{p}}\boldsymbol{H}^T(\boldsymbol{x}_{k+1}^{\mathrm{p}}) + \boldsymbol{Z}_{k+1}\big)^{-1}, \tag{16}$$

where the sensitivity matrix $\boldsymbol{H}(\boldsymbol{x}_k)$ represents the Jacobian matrix for (13b) which is defined as $\boldsymbol{H}(\boldsymbol{x}_k) = [\boldsymbol{H}_{k,F}^T \ \boldsymbol{H}_{k,B}^T]^T$ with

$$\boldsymbol{H}_{k,i} = \begin{bmatrix} \dfrac{\partial\tau_{k,i}}{\partial\boldsymbol{p}_k} & \dfrac{\partial\tau_{k,i}}{\partial\boldsymbol{v}_k} \\ \dfrac{\partial\theta_{k,i}}{\partial\boldsymbol{p}_k} & \dfrac{\partial\theta_{k,i}}{\partial\boldsymbol{v}_k} \\ \dfrac{\partial\phi_{k,i}}{\partial\boldsymbol{p}_k} & \dfrac{\partial\phi_{k,i}}{\partial\boldsymbol{v}_k} \end{bmatrix}$$

$$= \begin{bmatrix} \dfrac{1}{c_{\mathrm{avg}}d_{k,i}}(\boldsymbol{p}_k - \boldsymbol{b}_i)^T & \boldsymbol{0}_{1\times3} \\ \left[-\dfrac{\sin\theta_{k,i}}{d_{k,i}\cos\phi_{k,i}} \ \dfrac{\cos\theta_{k,i}}{d_{k,i}\cos\phi_{k,i}} \ 0 \right] & \boldsymbol{0}_{1\times3} \\ \left[-\dfrac{\cos\theta_{k,i}\sin\phi_{k,i}}{d_{k,i}} \ -\dfrac{\sin\theta_{k,i}\sin\phi_{k,i}}{d_{k,i}} \ \dfrac{\cos\phi_{k,i}}{d_{k,i}} \right] & \boldsymbol{0}_{1\times3} \end{bmatrix}, \tag{17}$$

for $i \in \{F, B\}$. By using Kalman gain $\boldsymbol{K}_{k+1}$, the state and covariance estimates are updated from their predictions $\boldsymbol{x}_{k+1}^{\mathrm{p}}$ and $\boldsymbol{P}_{k+1}^{\mathrm{p}}$ in (14) to

$$\boldsymbol{x}_{k+1}^{\mathrm{u}} = \boldsymbol{x}_{k+1}^{\mathrm{p}} + \boldsymbol{K}_{k+1}\big(\boldsymbol{y}_{k+1} - \boldsymbol{h}(\boldsymbol{x}_{k+1}^{\mathrm{p}})\big), \tag{18a}$$

$$\boldsymbol{P}_{k+1} = \big(\boldsymbol{I}_{6\times6} - \boldsymbol{K}_{k+1}\boldsymbol{H}(\boldsymbol{x}_{k+1}^{\mathrm{p}})\big)\boldsymbol{P}_{k+1}^{\mathrm{p}}. \tag{18b}$$

Finally, the $(k+1)$th WCE's position can be obtained as $\hat{\boldsymbol{p}}_{k+1} = [\boldsymbol{x}_{k+1}^{\mathrm{u}}]_{1:3}$ at each kth iteration of Algorithm 1, for $k = 0, \ldots, K-1$, where $\hat{\boldsymbol{p}}_k$ is the kth estimate of WCE's position.

4 Fundamental Limits of TOA/DOA and IMU-Based WCE Hybrid Localization

Here, we derive the PCRB of the TOA/DOA and IMU-based hybrid localization summarized in Algorithm 1 as fundamental limits on localization accuracy. In Algorithm 1, since the posterior information from the previous state is required, which makes the observations no longer independent, we adopt the PCRB [20, 21]. The following derivation of the PCRB is similar with Algorithm 1, except the fact that the Fisher information matrix (FIM) is an objective of recursion.

The SPE ρ_k for the kth estimated position $\hat{\boldsymbol{p}}_k$ is defined and lower-bounded by the PCRB $\mathrm{tr}\{\boldsymbol{J}_{\boldsymbol{p}_k}^{-1}\}$ as follows:

$$\rho_k = E\left\{\|\hat{\boldsymbol{p}}_k - \boldsymbol{p}_k\|^2\right\} \geq \mathrm{tr}\{\boldsymbol{J}_{\boldsymbol{p}_k}^{-1}\}, \tag{19}$$

where $\boldsymbol{J}_{\boldsymbol{p}_k}$ is the equivalent FIM (EFIM) [11–14, 18] for the estimate $\hat{\boldsymbol{p}}_k$. To calculate the PCRB $\mathrm{tr}\{\boldsymbol{J}_{\boldsymbol{p}_k}^{-1}\}$ in (19), we first consider the joint probability density function (pdf) for (13) as

$$p(\boldsymbol{X}_k, \boldsymbol{Y}_k) = p(\boldsymbol{x}_0)\prod_{n=1}^{k}p(\boldsymbol{y}_n|\boldsymbol{x}_n)\prod_{m=1}^{k}p(\boldsymbol{x}_m|\boldsymbol{x}_{m-1}), \tag{20}$$

where $\boldsymbol{X}_k = [\boldsymbol{x}_0^T\cdots\boldsymbol{x}_k^T]^T$ and $\boldsymbol{Y}_k = [\boldsymbol{y}_0^T\cdots\boldsymbol{y}_k^T]^T$. The conditional probabilities $p(\boldsymbol{x}_k|\boldsymbol{x}_{k-1})$ and $p(\boldsymbol{y}_k|\boldsymbol{x}_k)$ follow from (13a) and (13b), respectively. Let $\boldsymbol{J}(\boldsymbol{X}_k)$ be the $6k\times6k$ FIM of $\boldsymbol{X}_k$ attained from the joint pdf in (20) and $\boldsymbol{J}(\boldsymbol{x}_k)$ be the FIM of $\boldsymbol{x}_k$, which is the 6×6 right-lower block of $\boldsymbol{J}(\boldsymbol{X}_k)$. When we decompose $\boldsymbol{X}_k$ into $\boldsymbol{X}_k = [\boldsymbol{X}_{k-1}^T \ \boldsymbol{x}_k^T]^T$, $\boldsymbol{J}(\boldsymbol{X}_k)$ can be expressed as

$$\boldsymbol{J}(\boldsymbol{X}_k) = \begin{bmatrix} \boldsymbol{J}_k^{11} & \boldsymbol{J}_k^{12} \\ \boldsymbol{J}_k^{21} & \boldsymbol{J}_k^{22} \end{bmatrix}$$

$$= \begin{bmatrix} E\{-\Delta_{\boldsymbol{X}_{k-1}}^{\boldsymbol{X}_{k-1}}\ln p(\boldsymbol{X}_k,\boldsymbol{Y}_k)\} & E\{-\Delta_{\boldsymbol{X}_{k-1}}^{\boldsymbol{x}_k}\ln p(\boldsymbol{X}_k,\boldsymbol{Y}_k)\} \\ E\{-\Delta_{\boldsymbol{x}_k}^{\boldsymbol{X}_{k-1}}\ln p(\boldsymbol{X}_k,\boldsymbol{Y}_k)\} & E\{-\Delta_{\boldsymbol{x}_k}^{\boldsymbol{x}_k}\ln p(\boldsymbol{X}_k,\boldsymbol{Y}_k)\} \end{bmatrix}, \tag{21}$$

where we have defined the operator of the first- and second-order partial derivatives as $\nabla_{\boldsymbol{x}} = [\partial/\partial x_1\cdots\partial/\partial x_n]^T$ and $\Delta_{\boldsymbol{x}}^{\boldsymbol{y}} = \nabla_{\boldsymbol{x}}\nabla_{\boldsymbol{y}}^T$, respectively, for the arbitrary vectors $\boldsymbol{x} =$

Algorithm 1 TOA/DOA and IMU-based WCE hybrid localization

Initialize $\boldsymbol{x}_0 = \boldsymbol{x}_0^{\mathrm{u}} = \mu_x$ upon detection of patient's mouth.
for $k = 0$ to $K - 1$, **do**
    Predict the state $\boldsymbol{x}_{k+1}^{\mathrm{p}}$ and error covariance matrix $\boldsymbol{P}_{k+1}^{\mathrm{p}}$ using (14).
    Compute the Kalman gain $\boldsymbol{K}_{k+1}$ using (16).
    Update the state $\boldsymbol{x}_{k+1}^{\mathrm{u}}$ and error covariance matrix $\boldsymbol{P}_{k+1}$ using (18).
end
Output: Estimated WCE's position $\{\hat{\boldsymbol{p}}_k = [\boldsymbol{x}_k^{\mathrm{u}}]_{1:3}\}_{k=1,\ldots,K}$

$[x_1 \cdots x_n]^T$ and $\boldsymbol{y} = [y_1 \cdots y_n]^T$. By applying the Schur complement [22], the FIM $\boldsymbol{J}(\boldsymbol{x}_k)$ can be given as

$$\boldsymbol{J}(\boldsymbol{x}_k) = \boldsymbol{J}_k^{22} - \boldsymbol{J}_k^{21}(\boldsymbol{J}_k^{11})^{-1}\boldsymbol{J}_k^{12}, \qquad (22)$$

with $\boldsymbol{J}_k^{21} = (\boldsymbol{J}_k^{12})^T$. Then, we can write the $(k+1)$th joint pdf $p(\boldsymbol{X}_{k+1}, \boldsymbol{Y}_{k+1})$ as

$$\begin{aligned} p(\boldsymbol{X}_{k+1}, \boldsymbol{Y}_{k+1}) &= p(\boldsymbol{X}_k, \boldsymbol{Y}_k)p(\boldsymbol{x}_{k+1}|\boldsymbol{X}_k, \boldsymbol{Y}_k)p(\boldsymbol{y}_{k+1}|\boldsymbol{x}_{k+1}, \boldsymbol{X}_k, \boldsymbol{Y}_k) \\ &= p(\boldsymbol{X}_k, \boldsymbol{Y}_k)p(\boldsymbol{x}_{k+1}|\boldsymbol{x}_k)p(\boldsymbol{y}_{k+1}|\boldsymbol{x}_{k+1}), \end{aligned} \qquad (23)$$

which yields

$$\boldsymbol{J}(\boldsymbol{X}_{k+1}) = \begin{bmatrix} \boldsymbol{J}_k^{11} & \boldsymbol{J}_k^{12} & \boldsymbol{0} \\ \boldsymbol{J}_k^{21} & \boldsymbol{J}_k^{22} + \boldsymbol{D}_k^{11} & \boldsymbol{D}_k^{12} \\ \boldsymbol{0} & \boldsymbol{D}_k^{21} & \boldsymbol{D}_k^{22} \end{bmatrix}, \qquad (24)$$

where

$$\boldsymbol{D}_k^{11} = E\{-\Delta_{\boldsymbol{x}_k}^{\boldsymbol{x}_k}\ln p(\boldsymbol{x}_{k+1}|\boldsymbol{x}_k)\} = \boldsymbol{A}^T\boldsymbol{Q}^{-1}\boldsymbol{A}, \qquad (25a)$$

$$\boldsymbol{D}_k^{12} = E\{-\Delta_{\boldsymbol{x}_k}^{\boldsymbol{x}_{k+1}}\ln p(\boldsymbol{x}_{k+1}|\boldsymbol{x}_k)\} = -\boldsymbol{A}^T\boldsymbol{Q}^{-1}, \qquad (25b)$$

$$\boldsymbol{D}_k^{21} = E\{-\Delta_{\boldsymbol{x}_{k+1}}^{\boldsymbol{x}_k}\ln p(\boldsymbol{x}_{k+1}|\boldsymbol{x}_k)\} = -\boldsymbol{Q}^{-1}\boldsymbol{A} = (\boldsymbol{D}_k^{12})^T, \qquad (25c)$$

According to the matrix inversion lemma, we have the following equality relationship

$$\begin{aligned} \left(\boldsymbol{Q} + \boldsymbol{A}\boldsymbol{J}^{-1}(\boldsymbol{x}_k)\boldsymbol{A}^T\right)^{-1} = &\boldsymbol{Q}^{-1} \\ &- \boldsymbol{Q}^{-1}\boldsymbol{A}\left(\boldsymbol{J}(\boldsymbol{x}_k) + \boldsymbol{A}^T\boldsymbol{Q}^{-1}\boldsymbol{A}\right)^{-1}\boldsymbol{A}^T\boldsymbol{Q}^{-1}, \end{aligned} \qquad (27)$$

which allows us to rewrite $\boldsymbol{J}(\boldsymbol{x}_{k+1})$ as

$$\begin{aligned} \boldsymbol{J}(\boldsymbol{x}_{k+1}) = &E\{\boldsymbol{H}(\boldsymbol{x}_{k+1})^T\boldsymbol{Z}_{k+1}^{-1}\boldsymbol{H}(\boldsymbol{x}_{k+1})\} \\ &+ \left(\boldsymbol{Q} + \boldsymbol{A}\boldsymbol{J}^{-1}(\boldsymbol{x}_k)\boldsymbol{A}^T\right)^{-1}. \end{aligned} \qquad (28)$$

Note that the expectation with respect to the channel in (28) needs to be taken over Monte Carlo simulations. By following (28), we calculate the FIM $\boldsymbol{J}(\boldsymbol{x}_k)$ recursively until $k = K$ with initializing $\boldsymbol{J}(\boldsymbol{x}_0) = (\boldsymbol{P}_0)^{-1}$. Based on the Schur complement [22], the PCRB $\text{tr}\{\boldsymbol{J}_{\boldsymbol{p}_k}^{-1}\}$ for the estimated WCE's position $\hat{\boldsymbol{p}}_k$ by Algorithm 1 is therefore derived with the EFIM

$$\boldsymbol{J}_{\boldsymbol{p}_k} = [\boldsymbol{J}(\boldsymbol{x}_k)]_{(1:3,1:3)} - [\boldsymbol{J}(\boldsymbol{x}_k)]_{(1:3,4:6)}([\boldsymbol{J}(\boldsymbol{x}_k)]_{(4:6,4:6)})^{-1}[\boldsymbol{J}(\boldsymbol{x}_k)]_{(4:6,1:3)}, \qquad (29)$$

for $k = 1, \ldots, K$, where $[\cdot]_{(a:b,c:d)}$ is the sub-matrix of its argument corresponding to from the ath to the bth rows and from the cth to the dth columns. The process of the PCRB calculation is summarized in Algorithm 2.

Algorithm 2 PCRB calculation

Initialize $\boldsymbol{x}_0 = \boldsymbol{x}_0^u = \mu_x$ and $\boldsymbol{J}(\boldsymbol{x}_0) = (\boldsymbol{P}_0)^{-1}$ upon detection of patient's mouth.
for $k = 0$ to $K - 1$, **do**
 Compute the FIM $\boldsymbol{J}(\boldsymbol{x}_{k+1})$ of $\boldsymbol{x}_{k+1}$ using (28).
 Compute the PCRB $\text{tr}\{\boldsymbol{J}_{\boldsymbol{p}_{k+1}}^{-1}\}$ using (29).
end
Output: PCRB $\text{tr}\{\boldsymbol{J}_{\boldsymbol{p}_k}^{-1}\}_{k=1,\ldots,K}$ of the estimate $\{\hat{\boldsymbol{p}}_k\}_{k=1,\ldots,K}$ by Algorithm 1

$$\begin{aligned} \boldsymbol{D}_k^{22} &= E\{-\Delta_{\boldsymbol{x}_{k+1}}^{\boldsymbol{x}_{k+1}}\ln p(\boldsymbol{x}_{k+1}|\boldsymbol{x}_k)\} + E\{-\Delta_{\boldsymbol{x}_{k+1}}^{\boldsymbol{x}_{k+1}}\ln p(\boldsymbol{y}_{k+1}|\boldsymbol{x}_{k+1})\} \\ &= \boldsymbol{Q}^{-1} + E\{\boldsymbol{H}(\boldsymbol{x}_{k+1})^T\boldsymbol{Z}_{k+1}^{-1}\boldsymbol{H}(\boldsymbol{x}_{k+1})\}. \end{aligned} \qquad (25d)$$

Similarly with the previous step, by using the Schur complement [22], the FIM $\boldsymbol{J}(\boldsymbol{x}_{k+1})$ is represented as

$$\begin{aligned} \boldsymbol{J}(\boldsymbol{x}_{k+1}) &= \boldsymbol{D}_k^{22} - \begin{bmatrix} \boldsymbol{0} & \boldsymbol{D}_k^{21} \end{bmatrix}\begin{bmatrix} \boldsymbol{J}_k^{11} & \boldsymbol{J}_k^{12} \\ \boldsymbol{J}_k^{21} & \boldsymbol{J}_k^{22} + \boldsymbol{D}_k^{11} \end{bmatrix}^{-1}\begin{bmatrix} \boldsymbol{0} \\ \boldsymbol{D}_k^{12} \end{bmatrix} \\ &= \boldsymbol{D}_k^{22} - \boldsymbol{D}_k^{21}\left(\boldsymbol{J}_k^{22} + \boldsymbol{D}_k^{11} - \boldsymbol{J}_k^{21}(\boldsymbol{J}_k^{11})^{-1}\boldsymbol{J}_k^{12}\right)^{-1}\boldsymbol{D}_k^{12} \\ &= \boldsymbol{D}_k^{22} - \boldsymbol{D}_k^{21}\left(\boldsymbol{J}(\boldsymbol{x}_k) + \boldsymbol{D}_k^{11}\right)^{-1}\boldsymbol{D}_k^{12} \\ &= \boldsymbol{Q}^{-1} + E\{\boldsymbol{H}(\boldsymbol{x}_{k+1})^T\boldsymbol{Z}_{k+1}^{-1}\boldsymbol{H}(\boldsymbol{x}_{k+1})\} \\ &\quad - \boldsymbol{Q}^{-1}\boldsymbol{A}\left(\boldsymbol{J}(\boldsymbol{x}_k) + \boldsymbol{A}^T\boldsymbol{Q}^{-1}\boldsymbol{A}\right)^{-1}\boldsymbol{A}^T\boldsymbol{Q}^{-1}. \end{aligned} \qquad (26)$$

5 Numerical Results

In this section, we evaluate the performance of the TOA/DOA and IMU-based WCE hybrid localization in Sect. 3 by comparing with the derived PCRB in Sect. 4 via Monte Carlo simulations. For reference, we consider only RF (TOA/DOA)-based localization, only IMU-based localization, and two types of hybrid localizations, such as TOA and IMU-based localization and DOA and IMU-based localization. The reference hybrid localizations and their PCRBs are similarly developed by following Sects. 3 and 4, where the measurement model $\boldsymbol{y}_{k,i} = [\tau_{k,i}]$ is considered with the noise covariance matrix $\boldsymbol{Z}_{k,i} = \sigma_{\tau_{k,i}}^2$ and the sensitivity matrix $\boldsymbol{H}(\boldsymbol{x}_k)$ consisting of $\boldsymbol{H}_{k,i} = [\partial\tau_{k,i}/\partial\boldsymbol{p}_k \; \partial\tau_{k,i}/\partial\boldsymbol{v}_k]$ in the TOA and IMU-based localization, while, in the DOA and IMU-based localization, $\boldsymbol{y}_{k,i} =$

$[\theta_{k,i} \; \phi_{k,i}]^T$ with $\mathbf{Z}_{k,i} = \mathrm{diag}\{\sigma^2_{\theta_{k,i}}, \sigma^2_{\phi_{k,i}}\}$ and $\mathbf{H}(\mathbf{x}_k)$ consisting of $\mathbf{H}_{k,i} = [\partial\theta_{k,i}/\partial\mathbf{p}_k \; \partial\theta_{k,i}/\partial\mathbf{v}_k \; ; \; \partial\phi_{k,i}/\partial\mathbf{p}_k \; \partial\phi_{k,i}/\partial\mathbf{v}_k]$ are applied, for $i \in \{F, B\}$.

The NM sensors are assumed to be located in the front and back side of the patient's jacket with $L_W = L_L = L_H = 40$ cm and their reference positions $\mathbf{b}_F = [-20 \; 20 \; -50]^T$ (cm) and $\mathbf{b}_B = [-20 \; -20 \; -50]^T$ (cm), while the WCE's three-dimensional synthetic tract map is given in Fig. 2, which is obtained based on human digestive image in [9, 10]. The WCE initial conditions are $\mathbf{p}_0 = [0 \; 8 \; 0]$ (cm) and $\mathbf{v}_0 = [0 \; 0 \; 0]^T$ (cm/s), respectively, where the initial state error variances are 5 cm² for position and 0.1 cm²/s² for velocity [10]. We set $f_c = 405$ MHz to be consistent with MICS standard and noise level as $N_0 = -121$ dBm/Hz [11]. The small-scale fading channel coefficients $h^S_{k,i}$ are assumed to be independent and zero-mean complex Gaussian random variables with unit variance, while the large-scale fading follows the propagation model in (2) with the parameters of Table 1 corresponding to the distance $d_{k,i}$ between the kth WCE state and URA i, for $i \in \{F, B\}$. We assume that the EKF sampling time is $\delta = 1$ s and the signal propagation speed inside human is $c_{\mathrm{avg}} = 2.14 \times 10^8$ m/s [8]. Unless stated otherwise, we consider these parameters in the following. For the performance comparison, the root mean square (RMS) error is employed as

$$\mathrm{RMS\,error} = \sqrt{\frac{1}{N}\sum_{n=1}^{N}(\hat{\mathbf{p}}_k(n) - \mathbf{p}_k)^2}, \qquad (30)$$

where $\hat{\mathbf{p}}_k(n)$ is the estimated kth position of the WCE in the nth Monte Carlo experiments with N being the total number of experiments, which is compared with the square root of PCRB $\sqrt{\mathrm{tr}\{\mathbf{J}^{-1}_{\mathbf{p}_k}\}}$. Then, their mean values are evaluated by averaging across the WCE's samples from the initial time to the final time of the examination. It is reminded that no patient's body motion is assumed during the examination which can be justified by the fact that the estimation error due to the patient's motion can be mitigated by tracking the overall movements with the additional installation of the transmitters on the body. Accordingly, the WCE position estimated by the proposed algorithm can be mapped into the body reference frame.

First, we illustrate the mean RMS errors as a function of the WCE's transmit power P_t with $N = M = 5$ in Fig. 3 and as a function of the number of body-mounted sensors $N = M$ with $P_t = -16$ dBm in Fig. 4, respectively, when the acceleration measurement error standard deviation $\sigma_{\mu_u} = 0.03$ cm/s and the effective bandwidth $\beta = 300$ MHz are considered. As the transmit power P_t becomes larger and the number of sensors, namely NM,

increases, the localization accuracy of Algorithm 1 significantly increases up to submillimeter accuracy due to the improvement on the accuracy of RF measurements, and approaches closely to the PCRB. Moreover, the proposed Algorithm 1 outperforms all the reference localizations, and all the hybrid localizations based on both RF and IMU measurements, i.e., TOA and IMU-based, DOA and IMU-based and TOA/DOA and IMU-based methods, provide the higher localization accuracy than only RF-based and only IMU-based localization. From this, the hybrid localization using RF and IMU measurements can be seen to be preferred if the accuracies of the RF and IMU measurements are acceptable.

Note that, in the following, the WCE's transmit power is set to be $P_t = -16$ dBm due to the MICS regulation that a maximum transmit power of implanted medical devices is limited to -16 dBm so as to prevent the interference with other users of the same band. As shown in Fig. 3, the gap between the numerical and analytical performance in the available transmit power range $P_t \leq -16$ dBm is small enough in not only the TOA/DOA and IMU-based hybrid localization but also the TOA and IMU-based and the DOA and IMU-based hybrid localization, from which the derived PCRB is a proper criterion to quantify the localization accuracy.

In addition, the further performance improvements can be attained by increasing the effective bandwidth β in the localization techniques based on time measurements such as only RF-based, TOA and IMU-based and TOD/DOA and IMU-based methods as illustrated in Fig. 5, where the mean RMS errors are shown with the different values of effective bandwidth β when $N = M = 5, P_t = -16$ dBm and $\sigma_{\mu_u} = 0.03$ cm/s are considered.

Figure 6 shows the mean RMS errors as a function of the acceleration measurement error standard deviation σ_{μ_u} with $P_t = -16$ dBm, $\beta = 300$ MHz and $N = M = 5$. Compared to the above figures that show the dependency of the performance of Algorithm 1 on the accuracy of RF measurements, its dependency on the accuracy of IMU measurements can be here observed. Both numerical and analytical performances of schemes based on IMU measurements are degraded as σ_{μ_u} increases, especially for TOA and IMU-based localization. By incorporating the IMU measurements with two types of RF measurements in Algorithm 1, the robustness against the IMU measurements' error can be obtained while simultaneously the localization accuracy is enhanced. In a similar manner, the robustness against the inaccurate RF measurements can be also attained by integrating with the IMU measurements in the proposed scheme.
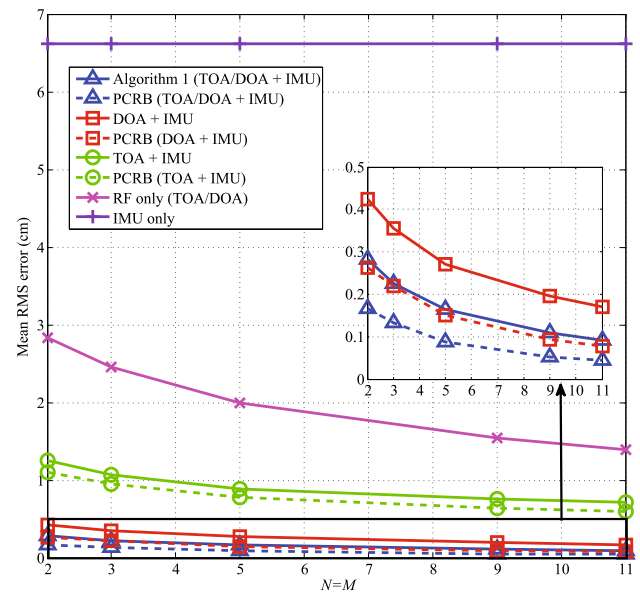
The mean RMS error as a function of the width L_W of URAs is shown in Fig. 7 with $P_t = -16$ dBm, $N = M = 5, \sigma_{\mu_u} = 0.03$ cm/s, $L_L = L_H = 40$ cm, $\mathbf{b}_F = [-L_W/2 \; 20$

Fig. 2 Three-dimensional synthetic tract map of the WCE ($N = M = 5$)
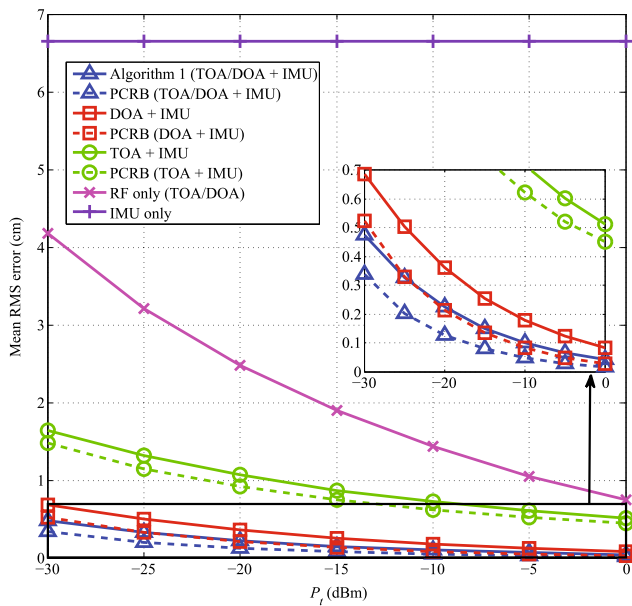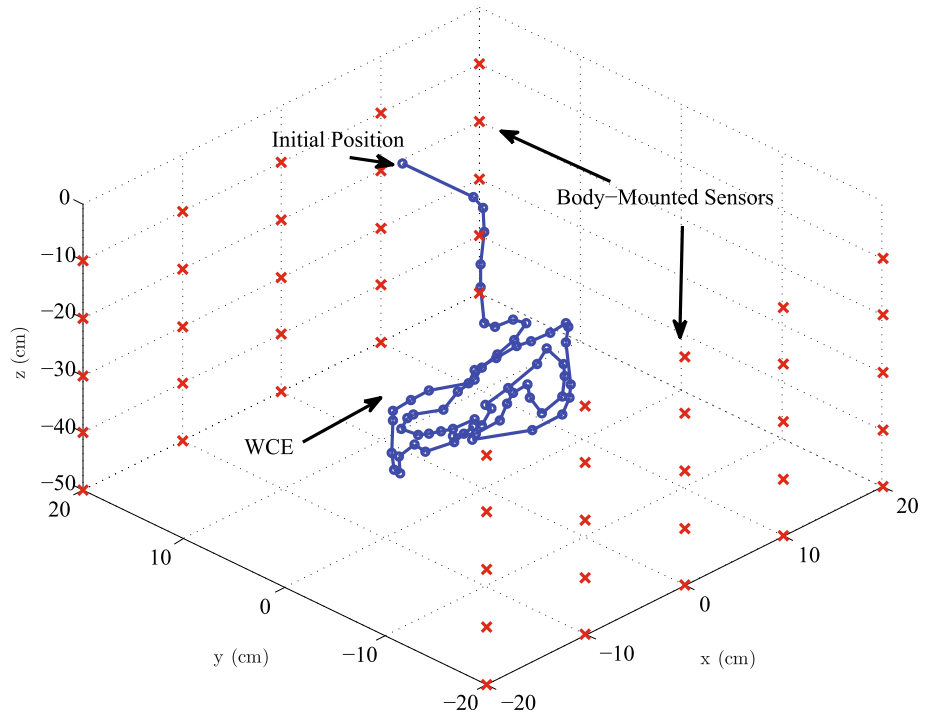
Fig. 3 Mean RMS error as a function of the WCE's transmit power P_t with $N = M = 5$, $\beta = 300$ MHz and $\sigma_{\mu_u} = 0.03$ cm/s

Fig. 4 Mean RMS error as a function of the number of sensors N (=M) with $P_t = -16$ dBm, $\beta = 300$ MHz and $\sigma_{\mu_u} = 0.03$ cm/s

$-50]^T$ (cm) and $\boldsymbol{b}_B = [-L_W/2 \ -20 \ -50]^T$ (cm). In Fig. 7, it is observed that the choice of the size and configuration of sensors noticeably affects both the numerical and analytical performance of Algorithm 1. Therefore, the optimal sensor configuration needs to be selected so as to provide the minimal localization error (Here, the optimal width is $L_W = 40$ cm in both numerical and analytical
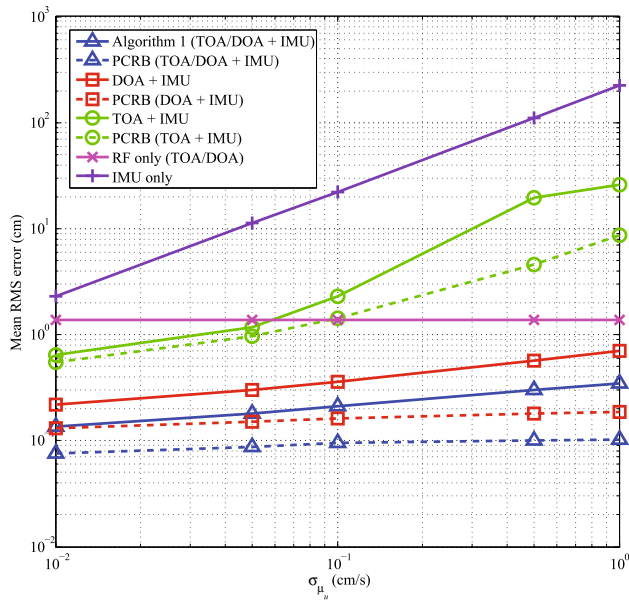
results), for which it is expected that the PCRB can provide the insight into the choice.

In Table 2, we describe the comparative accuracy of the WCE localization methods in terms of the mean drift per each meter traveled by the WCE with $N = M = 5$, $P_t = -16$ dBm, $\beta = 300$ MHz, and $\sigma_{\mu_u} = 0.03$ cm/s. The mean drift in traveled length is calculated as the summation of the mean errors of the estimated kth WCE's
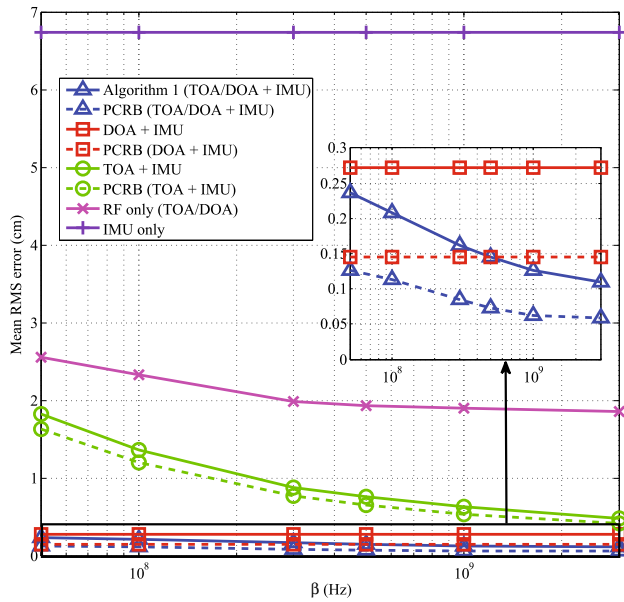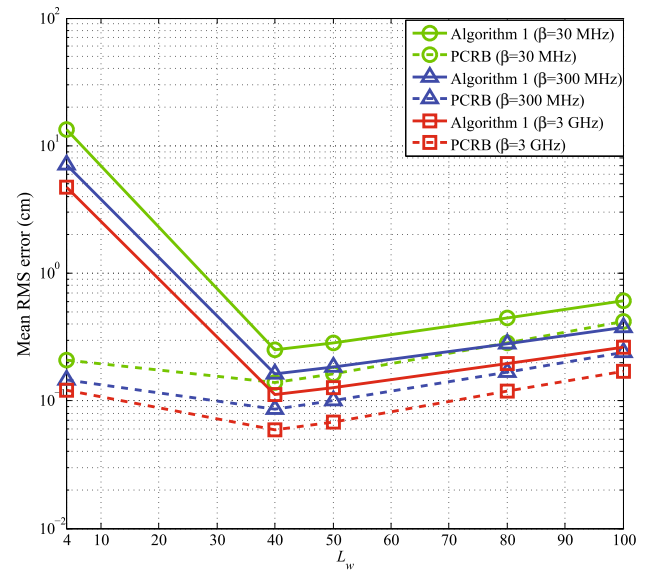
Fig. 5 Mean RMS error as a function of the effective bandwidth β with $N = M = 5, P_t = -16$ dBm and $\sigma_{\mu_u} = 0.03$ cm/s

Fig. 6 Mean RMS error as a function of the acceleration measurement error standard deviation σ_{μ_u} with $P_t = -16$ dBm, $\beta = 300$ MHz and $N = M = 5$

Fig. 7 Mean RMS error as a function of the width L_W of URAs with $P_t = -16$ dBm, $N = M = 5, \sigma_{\mu_u} = 0.03$ cm/s, $L_L = L_H = 40$ cm, $\boldsymbol{b}_F = [-L_W/2\ 20\ -50]^T$ (cm) and $\boldsymbol{b}_B = [-L_W/2\ -20\ -50]^T$ (cm)

achieve the mean drift of 0.157 cm per each meter traveled by the WCE, and the reference RF and IMU-based schemes also provide the mean drift less than 1 cm.

6 Concluding remarks

In this paper, we have studied the performance of TOA/DOA and IMU-based WCE hybrid localization for a single WCE traveling the GI tract. Particularly, two types of RF measurements, namely TOA and DOA, are combined with the IMU acceleration measurements via the EKF, which enables the high-performance WCE tracking. The fundamental limits on localization accuracy of the proposed TOA/DOA and IMU-based hybrid localization are derived by means of the PCRB, where the dependency of the accuracies of TOA and DOA measurements on environmental parameters is taken into account based on the CRB, while the accuracies of IMU measurements are addressed with the acceleration measurement error standard deviation. Numerical results validate the millimeter accuracy of the TOA/DOA and IMU-based hybrid localization within the MICS regulation and the exactness of the derived PCRB. It is noted that patient's body motion may create the estimation error, but it can be alleviated by motion tracking via the additional transmitter installed on the body. In addition, the proposed scheme can be readily extended with other sensor configurations or different types of position-related measurements. Therefore, interesting open problems concern the study about the optimal configuration of sensors to maximize the localization accuracy and the

position across the Monte Carlo experiments divided by the summation of the traveled length until kth WCE position, where the summation is operated from the initial to the final time of the experiment, i.e., from $k = 1$ to $k = K$. The exceptional performances of the proposed TOA/DOA and IMU-based hybrid localization as well as of the other reference RF and IMU-based hybrid schemes are striking, which verifies their applicability to the capsule endoscopy inspection in real life. For instance, Algorithm 1 can

Table 2 The comparative accuracy of WCE localization methods with $N = M = 5$, $P_t = -16$ dBm, $\beta = 300$ MHz, and $\sigma_{\mu_u} = 0.03$ cm/s

Algorithms	Mean drift per each meter traveled by the WCE (cm/m)
Algorithm 1 (TOA/DOA + IMU)	0.1570
DOA + IMU	0.2657
TOA + IMU	0.8400
RF only (TOA/DOA)	1.9045
IMU only	7.1535

performance analysis of the hybrid RF and IMU-based localization under the asynchronous assumption between the WCE and sensors.

References

1. A. K. Hara, J. A. Leighton, V. K. Sharma, R. I. Heigh and D. E. Fleischer, Small bowel: Preliminary comparison of capsule endoscopy with barium study and CT, *Radiology*, Vol. 230, No. 1, pp. 260–265, 2004.

2. G. Costamagna, S. Shah, M. Riccioni, F. Foschia, M. Mutignani, V. Perri, A. Vecchioli, M. Brizi, A. Picciocchi and P. Marano, A prospective trial comparing small bowel radiographs and video capsule endoscopy for suspected small bowel disease, *Gastroenterology*, Vol. 123, No. 4, pp. 999–1005, 2002.

3. G. Iddan, G. Meron and A. Glukhovsky, Wireless capsule endoscopy, *Nature*, Vol. 405, pp. 21–26, 2000.

4. X. Chen, S. Tamura, D. Lin and Y. Du, A 3D localization and navigation method for endoscope by magnetic field, *J. Comput. Res. Develop.*, Vol. 39, No. 2, pp. 242–246, 2002.

5. X. Guo, G. Yan, W. He and P. Jiang, Improved modeling of electromagnetic localization for implantable wireless capsules, *Biomed. Instrum. Technol.*, Vol. 44, No. 4, pp. 354–359, 2010.

6. L. Liu, C. Hu, W. Cai, M.Q.H. Meng, Capsule endoscope localization based on computer vision technique, In: Proc. Annu. Int. Conf. IEEE Eng. Med. Biol. Soc. (EMBC), pp. 3711–3714, 2009.

7. J. Bulat, K. Duda, M. Duplaga, R. Fraczek, A. Skalski, M. Socha, P. Turcza, T. Zielinski, Data processing tasks in wireless GI endoscopy: Image-based capsule localization & navigation and video compression, In: Proc. Annu. Int. Conf. IEEE Eng. Med. Biol. Soc. (EMBC), pp. 2815–2818, 2007.

8. Y. Geng and K. Pahlavan, Design, implementation and fundamental limits of image and RF based wireless capsule endoscopy hybrid localization, *IEEE Transactions on Mobile Computing*, Vol. 15, No. 8, pp. 1951–1964, 2016.

9. A. Nafchi, S. Goh, R. Zekavat and A. Seyed, Circular arrays and inertial measurement unit for DOA/TOA/TDOA-based endoscopy capsule localization: Performance and complexity investigation, *IEEE Sensors Journal*, Vol. 14, No. 11, pp. 3791–3799, 2014.

10. S. Goh, R. Zekavat, A. Seyed and K. Pahlavan, DOA-based endoscopy capsule localization and orientation estimation via unscented kalman filter, *IEEE Sensors Journal*, Vol. 14, No. 11, pp. 3819–3829, 2014.

11. S. Jeong, O. Simeone, A. Haimovich and J. Kang, Beamforming design for joint localization and data transmission in distributed antenna system, *IEEE Trans. Veh. Technol.*, Vol. 64, No. 1, pp. 62–76, 2015.

12. S. Jeong, O. Simeone, A. Haimovich and J. Kang, Optimal fronthaul quantization for cloud radio positioning, *IEEE Trans. Veh. Technol.*, Vol. 65, No. 4, pp. 2763–2768, 2016.

13. S. Jeong, O. Simeone, A. Haimovich and J. Kang, Positioning via Direct Localization in C-RANs Systems, *IET Communications*, Vol. 10, No. 16, pp. 2238–2244, 2016.

14. S. Jeong, T. Sung, K. Lee, J. Kang, Joint TOA/AOA-based localization in wireless sensor networks, In: Proc. Int. Conf. IEEE Signal Processing and Communication Systems (ICSPCS), 2014.

15. IEEE 802.15 Tg6, Draft of channel model for body area network, 2010.

16. K. Yazdandoost, K. Sayrafian-Pour, Channel model for body area network (BAN), IEEE 802.15 Working Group Document, IEEE P802, 2009.

17. R. A. Barnett, M. R. Ziegler, K. E. Byleen and D. Sobecki, *Analytic trigonometry with applications*, vol. 11th, Wiley, New York, 2011.

18. S. M. Kay, *Fundamentals of signal processing-estimation theory*, Prentice Hall, Englewood Cliffs, 1993.

19. J. L. Crassidis and J. L. Junkins, *Optimal estimation of dynamic systems*, vol. 2nd, CRC Press, London, 2011.

20. H. L. V. Trees, *Detection, estimation and modulation theory*, Wiley, New York, 1968.

21. P. Tichavský, C. Muravchik and A. Nehorai, Posterior Cramér–Rao bounds for discrete-time nonlinear filtering, *IEEE Trans. Sig. Proc.*, Vol. 46, No. 5, pp. 1386–1396, 1998.

22. F. Zhang, *The Schur complement and its applications* 4 ed., Springer, Berlin, 2005.

Seongah Jeong received the B.S. (magna cum laude), M.S., and Ph.D. degree from Korea Advanced Institute of Science and Technology (KAIST), Daejeon, Korea, in 2010, 2012 and 2015, respectively. She is currently a postdoctoral researcher with School of Engineering and Applied Sciences, Harvard University, Cambridge, MA, USA. In 2009, she was an intern with the Electria-Wireless Sensor Network Laboratory, Helsinki Metropolia University of Applied Sciences, Vantaa, Finland. From 2013 to 2014, she was a Visiting Scholar with the Center of Wireless Communications and Signal Processing Center, New Jersey Institute of Technology, Newark, NJ, USA. She was a postdoctoral researcher with Information and Electronics Research Institute, KAIST in 2015. She is a recipient of the Silver and Bronze Prize at the 21st and 20th Samsung Human-tech Paper Contest award in 2015 and 2014, respectively, and Annual Honor Roll Award for Excellent 3rd year Doctoral Student in Research Performance Evaluation System in KAIST. Her research interests include signal processing for biology, positioning in cloud-based networks, mobile cloud computing and physical-layer security.

Joonhyuk Kang (M'03) received the B.S.E. and M.S.E. degrees from Seoul National University, Seoul, Korea, in 1991 and 1993, respectively, and the Ph.D. degree in electrical and computer engineering from the University of Texas at Austin, Austin, TX, USA, in 2002. He is currently a Faculty Member with the Department of Electrical Engineering, Korea Advanced Institute of Science and Technology, Daejeon, Korea. From 1993 to 1998, he was a Research Staff with SAMSUNG Electronics, Suwon, Korea, where he was involved in the development of digital-signal-processing-based real-time control systems. In 2000, he was with Cwill Telecommunications, Austin, where he participated in the project for multicarrier code-division multiple-access systems with an antenna array. From 2008 to 2009, he was a Visiting Scholar with the School of Engineering and Applied Sciences, Harvard University, Cambridge, MA, USA. His research interests include signal processing for cognitive radio, cooperative communication, physical-layer security, and wireless localization. Dr. Kang is a member of the Korea Information and Communications Society and Tau Beta Pi (the Engineering Honor Society) and received the Texas Telecommunication Consortium Graduate Fellowship from 2000 to 2002.

Kaveh Pahlavan is a Professor of Electrical and Computer Engineering, a Professor of Computer Science, and the Director of the Center for Wireless Information Network Studies at the Worcester Polytechnic Institute, Worcester, MA, USA. His current area of research is localization for body area networks and robotics applications. He was a Westin Hadden Professor of ECE at WPI (1993–1996), a fellow of the IEEE (1996), a Nokia fellow (1999), a Fulbright-Nokia Scholar (2000), and the winner of WPI's board of trustee's best researcher award (2011). He has chaired a number of pioneering conferences and has written several books in the area of wireless networks.

Vahid Tarokh was with AT&T Labs-Research and AT&T wireless services until 2000, where he was the Head of the Department of Wireless Communications and Signal Processing. In 2000, he joined the Department of Electrical Engineering and Computer Sciences, MIT, as an Associate Professor. In 2002, he joined Harvard University as a Gordon McKay Professor of Electrical Engineering. Since 2005, he has been a Hammond Vinton Hayes Senior Fellow of Electrical Engineering with Harvard University. His output of the last 20 years is summarized in about 60 research journal papers that have been cited almost 40,000 times by other scholars. He is a recipient of a number of awards, and holds two honorary degrees.